catalysts

MDPI

Communication

One-Pot Synthesis of Highly Dispersed VO_2 on g-C_3N_4 Nanomeshes for Advanced Oxidation

Yangzhou Deng [1], Yuqi Zhang [1], Kunkun Wei [2], Yue Wang [2], Shihui Zou [2,*] and Juanjuan Liu [1,*]

[1] College of Materials & Environmental Engineering, Hangzhou Dianzi University, Hangzhou 310036, China
[2] Institute of Catalysis, Department of Chemistry, Zhejiang University, Hangzhou 310027, China
* Correspondence: xueshan199@zju.edu.cn (S.Z.); liujuanjuan0324@hdu.edu.cn (J.L.)

Abstract: Advanced oxidation catalyzed by metal oxides is a promising approach for degrading organic pollutants in wastewater. A critical strategy to enhance the performance of these catalysts is optimizing the dispersion of their active components through innovative synthesis methods. In this study, we report a one-pot synthesis of g-C_3N_4 nanomeshes supported with highly dispersed VO_2 catalysts (V-g-C_3N_4) for the advanced oxidation of methylene blue (MB). The characterization results reveal that the involvement of VCl_3 in the pyrolysis of melamine facilitates the formation of g-C_3N_4 nanomeshes with abundant amino groups (NH/NH_2). The strong interaction between vanadia species and amino groups prevents VO_2 particles from agglomerating, resulting in a significantly higher vanadia dispersion than V-g-C_3N_4-im synthesized via the traditional impregnation method. V-g-C_3N_4 exhibits a sophisticated microstructure and surface structure, which leads to a rate constant 2.3-fold higher than V-g-C_3N_4-im in the catalytic degradation of methylene blue using H_2O_2 as the oxidant. X-ray photoelectron spectroscopy, trapping experiments, and electron paramagnetic resonance measurements reveal that the rapid adsorption and fast diffusion of MB over g-C_3N_4 nanomeshes, together with the efficient H_2O_2 activation into ·OH radicals via the V^{4+}/V^{5+} redox cycle, synergistically contribute to the superior MB removal efficiency of V-g-C_3N_4. Moreover, V-g-C_3N_4 demonstrates no significant decrease in activity even after the fourth cycle, indicating its excellent stability during the pollutant removal process.

Keywords: advanced oxidation process; Fenton-like; g-C_3N_4; nanomesh; VO_2; dispersion

Citation: Deng, Y.; Zhang, Y.; Wei, K.; Wang, Y.; Zou, S.; Liu, J. One-Pot Synthesis of Highly Dispersed VO_2 on g-C_3N_4 Nanomeshes for Advanced Oxidation. *Catalysts* **2024**, *14*, 892. https://doi.org/10.3390/catal14120892

Academic Editor: Enric Brillas

Received: 4 November 2024
Revised: 29 November 2024
Accepted: 3 December 2024
Published: 4 December 2024

1. Introduction

Organic dyes are extensively utilized in the textile, printing, and paper industries [1,2]. These dyes, typically complex aromatic compounds with high persistence and visibility, can contaminate water bodies, disrupt aquatic ecosystems, and pose health risks to humans [3,4]. To mitigate the environmental threat, it is essential to neutralize or decompose these dyes from wastewater prior to their final discharge into the environment [5]. Among various water treatment processes, advanced oxidation processes (AOPs) stand out as an effective route for the purification of dye effluents [6–9]. This effectiveness stems from their ability to generate strongly oxidizing agents, such as •OH radicals [10,11]. The traditional Fenon reaction, which utilizes the efficient reaction between Fe^{2+} and H_2O_2 to generate •OH, is one of the most widely studied AOPs for degrading organic pollutants [11,12]. However, this process suffers from several limitations, including a narrow operating pH range, the unrecyclable use of excessive Fe^{2+}, and the generation of a significant volume of iron sludge [3]. To overcome these challenges, researchers have explored the use of heterogeneous Fenton-like catalysts [13–16], such as supported multivalent metal oxides (e.g., Fe, Mn, Co, Cu, V). For example, Zubir et al. [17] reported that well-dispersed iron oxide nanoparticles supported on graphene oxide sheets can be used as heterogeneous Fenton-like catalysts to rapidly degrade Acid Orange 7 dye. Ling et al. [18] demonstrated activated alumina-supported CoMnAl composite metal oxides as an efficient,

stable, and reusable Fenton-like catalyst for the detoxification of pharmaceutical wastewater in neutral condition. In addition, polymers loaded with iron oxide or copper have also been used as cost-effective Fenton catalysts to degrade organic pollutants [19]. Despite the advancements, the activity of these catalysts still has considerable room for improvement, which necessitates the innovation of synthesis methods to optimize their structures.

Metal oxides stabilized on supports are usually synthesized by physical methods (e.g., evaporation, sputtering) or chemical methods (e.g., ion exchange, co-precipitation, sol–gel, wet impregnation) [20,21]. The catalytic performances of metal oxides can be readily modulated by their size, dispersion, surface structures, and the interaction with the support [22]. With the development of nanotechnology, researchers have dedicated considerable effort to optimizing the dispersion of supported metal oxides [23], aiming to maximize the concentration of active sites and enhance their catalytic performance [22,24]. Among various factors, the choice of support and the method of synthesis are particularly important. Graphitic carbon nitride (g-C_3N_4) is commonly utilized as a two-dimensional (2D) support for metals and metal oxides, owing to its plentiful uncondensed aliphatic amines (NH_2 and -NH- groups) that act as anchoring sites for active species [25–28]. Nevertheless, g-C_3N_4 synthesized via conventional pyrolysis methods often exhibits a low surface-to-volume ratio and limited active sites, leading to the agglomeration of supported particles. Engineering sophisticated nanostructures for g-C_3N_4 can increase the surface area and provide more interaction sites to disperse metal oxides. However, traditional strategies of preparing g-C_3N_4 nanostructures with highly dispersed metal oxides often involve multiple steps, long synthesis times, and even the use of expensive equipment and reagents [28,29]. To meet the demand for time efficiency and sustainability, it is appealing to develop facile and environmentally friendly methods to disperse metal oxides on g-C_3N_4 under mild conditions. The one-pot protocol, which combines multiple reactions into a single reaction vessel, has significant potential to minimize the number of required steps, reduce complexity, and conserve time and resources. However, the intricate reactions among the reagents in one-pot synthesis pose challenges in achieving a high dispersion of metal oxides.

This study presents a one-pot synthesis method for V-g-C_3N_4 nanocatalysts, featuring highly dispersed VO_2 species on nanomesh-structured g-C_3N_4. Unlike the traditional method, which directly impregnates as-synthesized g-C_3N_4 in a VCl_3 solution, the one-pot synthesis method involves VCl_3 in the transformation of melamine into g-C_3N_4. The strong interaction between VCl_3 and the abundant amine groups in melamine enables the in situ conversion of VCl_3 and melamine into highly dispersed VO_2 and g-C_3N_4 nanomeshes with abundant amino groups (NH/NH_2) during pyrolysis. Due to its advanced microstructures and surface features, V-g-C_3N_4 demonstrates enhanced catalytic activity over V-g-C_3N_4-im in methylene blue degradation with H_2O_2 as the oxidant.

2. Results and Discussion

V-g-C_3N_4 nanostructures were synthesized via a method illustrated in Scheme 1. In this method, melamine and VCl_3 were mixed in one pot to fabricate g-C_3N_4-supported highly dispersed vanadia species. g-C_3N_4 was synthesized following the same steps as V-g-C_3N_4, except for the absence of VCl_3. V-g-C_3N_4-im was synthesized using a traditional impregnation method, with g-C_3N_4 and VCl_3 as the starting materials. XRD was used to analyze the chemical composition and crystalline structure of the samples. As shown in Figure 1a, all three samples display a peak at ~27.5°, corresponding to the (002) plane of g-C_3N_4 (JCPDS: 87–1526) [27,30]. Notably, the peak in V-g-C_3N_4 is significantly broader than those in g-C_3N_4 and V-g-C_3N_4-im, suggesting that the one-pot synthesis method induces a different microstructure for g-C_3N_4. The N_2 adsorption–desorption isotherms further confirm this observation (Figure 1b). All samples display type IV adsorption isotherms with H3 hysteresis loops, signifying the presence of mesopores. The larger hysteresis loop observed for V-g-C_3N_4 implies the presence of more mesopores compared to the other samples. This eventually leads to a large surfacer area of V-g-C_3N_4 (43 $m^2\ g^{-1}$) than g-C_3N_4 (10 $m^2\ g^{-1}$) and V-g-C_3N_4-im (27 $m^2\ g^{-1}$). Notably, characteristic XRD peaks

were also observed in V-g-C_3N_4-im at 33.0°, 36.2°, 41.2°, 53.9°, and 65.2°, which can be well indexed to the (104), (110), (113), (112), and (300) planes of V_2O_3 (JCPDS:34-0187) [31,32], respectively. In contrast, no obvious peaks related to vanadium oxides are observed in V-g-C_3N_4, probably due to the small particle size and good dispersion of vanadia species.

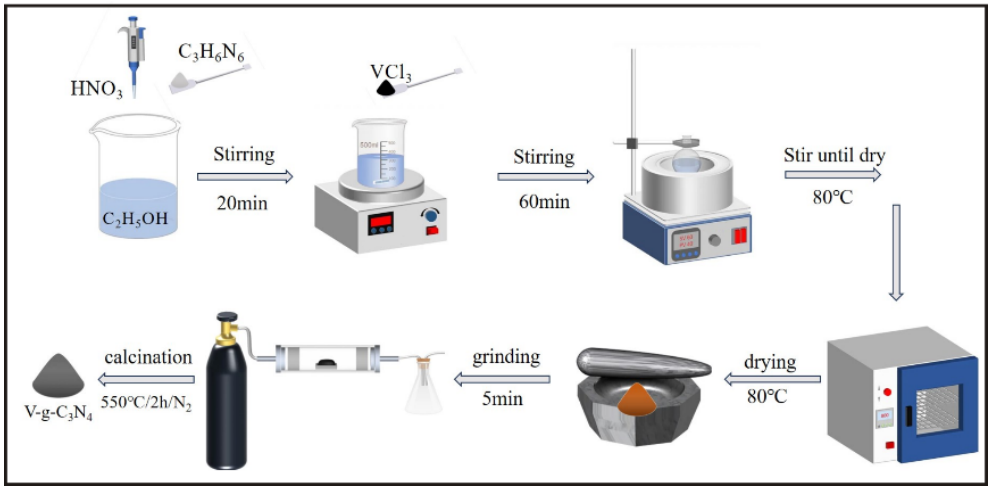

Scheme 1. Schematic illustration of the one-pot synthetic process for V-g-C_3N_4 nanostructures.

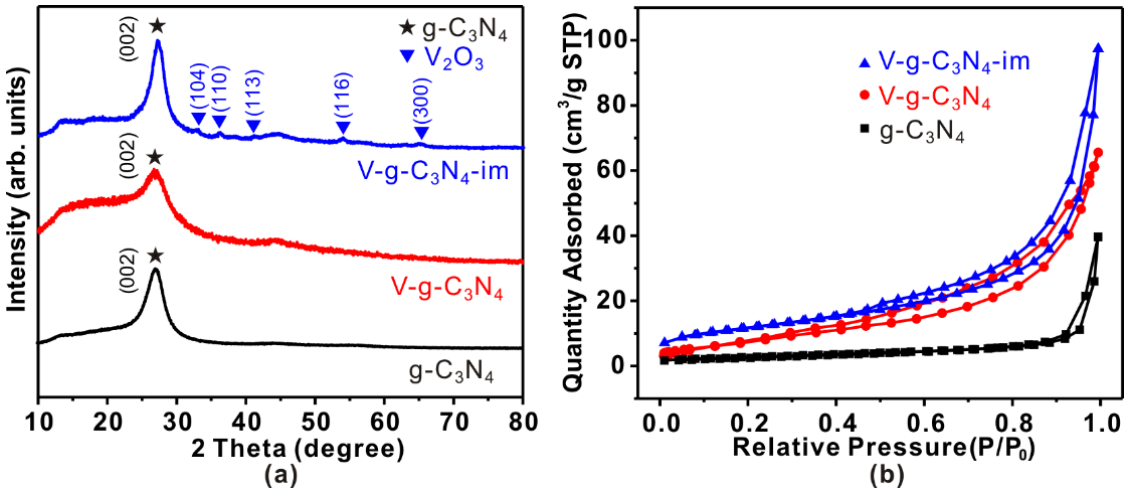

Figure 1. (**a**) XRD patterns and (**b**) N_2 adsorption–desorption isotherms of the g-C_3N_4, V-g-C_3N_4 and V-g-C_3N_4-im samples.

The microstructure and morphology of the synthesized samples were first examined using a SEM (Figure 2). In contrast to g-C_3N_4 and V-g-C_3N_4-im, which exhibit irregular bulk structures (Figure 2a,d), V-g-C_3N_4 displays a nanomesh structure with an interconnected network (Figure 2b,c). This suggests that the introduction of vanadium species during the g-C_3N_4 fabrication process influences the final framework, which is consistent with the XRD result and N_2 sorption isotherms. High-angle annular dark field scanning transmission electron microscopy (HAADF-STEM, Figure 2e) further confirms the nanomeshes structure of V-g-C_3N_4. Moreover, the EDX elemental mapping of V-g-C_3N_4 shows uniform distribution of C, N, and V across the sample. The absence of noticeable vanadia aggregation on the g-C_3N_4 surface indicates a high dispersion of vanadia species in V-g-C_3N_4, aligning well with the XRD results presented in Figure 1a.

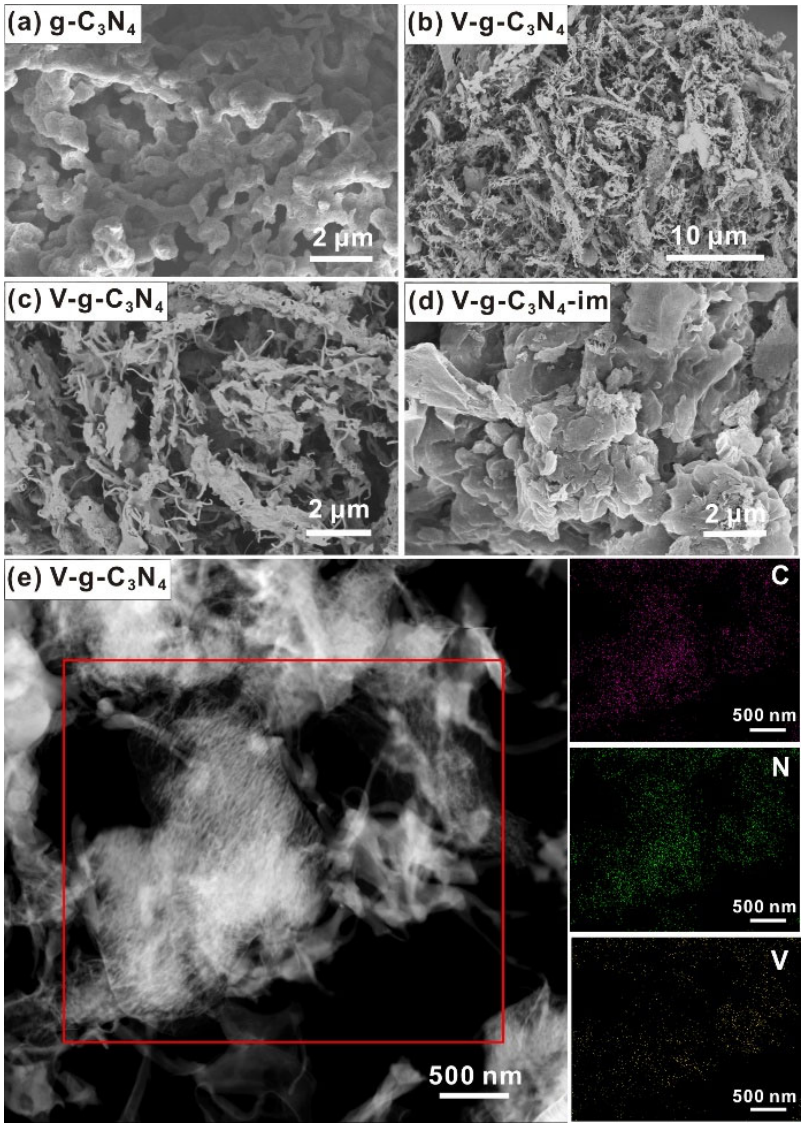

Figure 2. SEM images of the as-prepared (**a**) g-C_3N_4, (**b**,**c**) V-g-C_3N_4, and (**d**) V-g-C_3N_4-im. (**e**) HAADF-STEM and elemental mapping of V-g-C_3N_4.

V-g-C_3N_4 and V-g-C_3N_4-im not only have distinct microstructures, but also display different surface structures (Figure 3a). The N1s high-resolution XPS spectra for all samples reveal three deconvoluted peaks at 398.5 eV, 399.2 eV, and 400.6 eV, representing sp^2-hybridized triazine nitrogen (C-N=C, N_a), sp^3-hybridized three-coordinate N species (C-N(-C)-H and N-$(C)_3$, N_b), and sp^3-hybridized surface nitrogen pending amino groups (e.g., -NH_2, N_c in Figure 3b) at the edge of the g-C_3N_4 framework, respectively [33,34]. Interestingly, the percentages of N_a (57.5% vs. 57.1%), N_b (25.6% vs. 25.2%), and N_c (16.9% vs. 17.7%) in V-g-C_3N_4-im are almost identical to those in g-C_3N_4, indicating that the impregnation of V_2O_3 onto g-C_3N_4 does not significantly alter the structure of g-C_3N_4. Nevertheless, the relative contents of these N species are significantly different between V-g-C_3N_4 and V-g-C_3N_4-im. For V-g-C_3N_4, the percentage of N_a decreases to 48.4% while the percentage of N_b increases to 33.0%, indicating that the presence of vanadium species during the conversion of melamine to g-C_3N_4 induces structural changes in the surface heterocycles of g-C_3N_4. More three-coordinated N species are generated, providing anchoring sites for vanadium species and ultimately leading to a high dispersion of vanadia. These observations are consistent with the microstructural characterization shown in Figure 2.

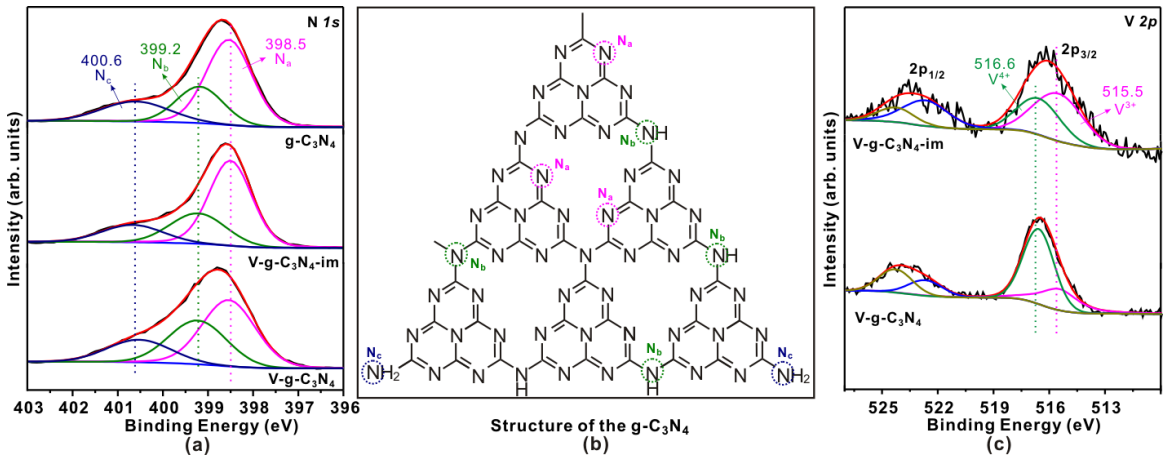

Figure 3. (**a**) XPS analysis of N1s; (**b**) the structure of the g-C_3N_4 and (**c**) XPS analysis of V2p in V-g-C_3N_4 and V-g-C_3N_4-im samples.

The preparation method not only alters the structure of g-C_3N_4, but also influences the surface chemical states of vanadium. Figure 3c shows the V2$p_{3/2}$ spectra of V-g-C_3N_4 and V-g-C_3N_4-im, which can be deconvoluted into two peaks at 515.5 and 516.6 eV, corresponding to V^{3+} and V^{4+}, respectively [35]. Interestingly, the relative content of V^{3+}/V^{4+} differs significantly. For V-g-C_3N_4-im, vanadium mainly exists as V_2O_3 (Figure 1a). Accordingly, V^{3+} (59.6%) dominates the surface. In stark contrast, V-g-C_3N_4 exhibits a V^{3+}/ V^{4+} ratio of 0.307/0.693, indicating that vanadium mainly exists as highly dispersed VO_2.

The distinct microstructures and surface structures between V-g-C_3N_4 and V-g-C_3N_4-im likely originate from the different interaction between VCl_3 and g-C_3N_4. Theoretically, strong interactions between precursors and supports facilitate high precursor dispersion, which in turn leads to a high dispersion of supported nanomaterials [33,36]. In terms of VCl_3, its interaction with amino groups is usually stronger than that with triazine nitrogen [33]. Therefore, when VCl_3 is mixed with melamine in the one-pot synthesis method, the abundant amino groups in melamine strongly bind to VCl_3, forming a complex with highly dispersed VCl_3. During the subsequent pyrolysis process, VCl_3 and melamine undergo in situ conversion to form vanadia and g-C_3N_4. This in situ conversion facilitates both the high dispersion of vanadium oxide and the formation of a nanomesh structure in g-C_3N_4 with a high N_b content. In contrast, g-C_3N_4 synthesized via melamine pyrolysis possesses a limited number of amino groups available for interaction with VCl_3 (Figure 3a). During the impregnation process, the weak interaction between VCl_3 and g-C_3N_4 hinders the uniform dispersion of VCl_3. Consequently, during the subsequent pyrolysis step, the agglomerated VCl_3 tends to form large V_2O_3 nanoparticles instead of highly dispersed VO_2 species. Meanwhile, the structure of g-C_3N_4 remains largely unaltered during this process. Notably, traditional strategies to prepare g-C_3N_4 nanostructures with highly dispersed metal oxides often involve multiple steps, long synthesis times, and even the use of expensive equipment and reagents [28,29,37]. In contrast, the one-pot protocol reported in this study minimizes the number of required steps, thereby reducing complexity and conserving both time and resources. This makes it an attractive option for the design and synthesis of new materials. It is crucial to emphasize that the successful implementation of the one-pot synthesis of V-g-C_3N_4 relies on a strong interaction between VCl_3 and melamine. This method may also be applicable to other metal oxide systems, provided that the interactions between the reagents are precisely controlled.

Methylene blue (MB), frequently found in industrial wastewater, presents considerable health hazards if not properly treated [38]. These risks include tissue necrosis, cyanosis, jaundice, vomiting, and shock [39]. Effective removal of MB from wastewater is necessary prior to industrial discharge to mitigate its negative effects. In this study, the catalytic activity of V-g-C_3N_4 was evaluated via MB removal with H_2O_2 at room temperature.

The adsorption of MB by the catalysts was examined before conducting the catalytic test. Figure 4a demonstrates that different materials show varying adsorption capacities for MB. V-g-C_3N_4 exhibits a notable adsorption efficiency of 34.9%, surpassing both pristine g-C_3N_4 (3.3%) and V-g-C_3N_4-im (19.5%). This enhancement is attributable to the increased surface area of V-g-C_3N_4. Notably, the catalysts also exhibit different behavior in the following catalysis. As demonstrated in Figure 4a, MB is stable and does not undergo self-degradation within 60 min in the absence of either H_2O_2 or catalyst. Upon adding 2 mL of H_2O_2 into the mixture, V-g-C_3N_4 demonstrates enhanced degradation activity relative to g-C_3N_4 and V-g-C_3N_4-im. Specifically, V-g-C_3N_4 demonstrated ~91% degradation of MB within 30 min, outperforming g-C_3N_4 and V-g-C_3N_4-im, which achieved only ~39.3% and ~65.7% removal efficiency, respectively, within the same time frame. The kinetic plots of the degradation results were well-fitted by the pseudo-first-order model. As shown in Figure 4b, the degradation rate constant on V-g-C_3N_4 was 0.056 min^{-1} (Figure 4c), which is 48.3, 4.3, and 2.3 times higher than that of the blank, pristine g-C_3N_4, and V-g-C_3N_4-im, respectively. These results clearly indicate that V-g-C_3N_4 with highly dispersed VO_2, exhibits better catalytic activity. The superior activity of V-g-C_3N_4 is likely attributed to the highly dispersed VO_2 nanoparticles in the framework of the g-C_3N_4 nanomeshes, in contrast to the aggregated V_2O_3 particles supported on the bulk g-C_3N_4. Furthermore, recycling experiments were conducted to evaluate the stability of V-g-C_3N_4 in removing MB. As displayed in Figure 4d, there is no significant decrease in activity even after the fourth cycle, indicating that the V-g-C_3N_4 composites are quite stable during the pollutant removal process.

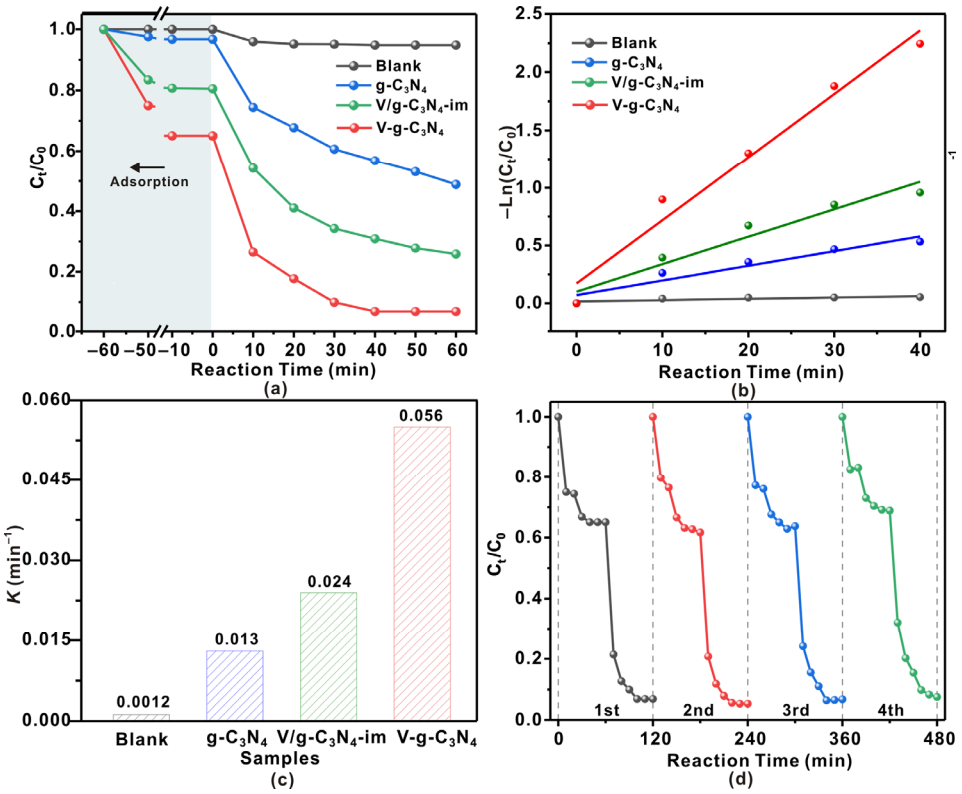

Figure 4. (**a**) Removal efficiencies of the MB over various catalysts; (**b**) kinetic linear simulation curves and (**c**) the corresponding reaction rate constants for various catalysts. (**d**) The reusability of V-g-C_3N_4 for MB removal.

Notably, the absence of either H_2O_2 or catalysts results in no MB degradation, indicating that MB is broken down by reactive oxygen species (ROS), such as ·OH or O_2^-, produced via a Fenton-like reaction between the H_2O_2 and the catalysts. To determine the dominant ROS involved in the V-g-C_3N_4 catalyzed MB removal process, trapping exper-

iments were conducted using p-benzoquinone to trap O_2^- and tert-butanol to trap ·OH radicals [40] (Figure 5a). Interestingly, the addition of p-benzoquinone after the mixture reached adsorption equilibrium has little effect on the degradation efficiency, implying that O_2^- radicals are not the primary ROS. In contrast, the degradation efficiency is significantly reduced upon the addition of tert-butanol, suggesting the essential role of ·OH radicals in the catalytic removal of MB. Electron paramagnetic resonance (EPR) measurements with 5,5-Dimethyl-1-Pyrroline-N-oxide (DMPO) as the trapping reagent further validated these findings. When V-g-C_3N_4 is mixed with H_2O_2 and DMPO, four antisymmetric peaks with an intensity ratio of 1:2:2:1 are observed (Figure 5b), characteristic of DMPO-·OH signals [40]. In stark contrast, no such signals are observed in the case of H_2O_2 + DMPO and H_2O_2+g-C_3N_4+DMPO. These results suggest that the primary ROS, ·OH, are produced via the reaction between H_2O_2 and the highly dispersed VO_2 species. According to the literature [41–43], both V^{4+} ($VO^{2+} + H_2O_2 \rightarrow VO_2^+ + {\cdot}OH + H+$) and V^{3+} ($V^{3+} + H_2O_2 \rightarrow VO^{2+} + {\cdot}OH + H^+$) can react with H_2O_2 to generate ·OH. In addition, the produced VO_2^+ species can be reduced to VO^{2+} to complete the V^{4+}/V^{5+} cycle (Figure 5c). To this end, supported vanadia with abundant V^{4+} species are widely used as Fenton-like catalysts for various applications, such as benzene hydroxylation and advanced oxidation of organic pollutants [33].

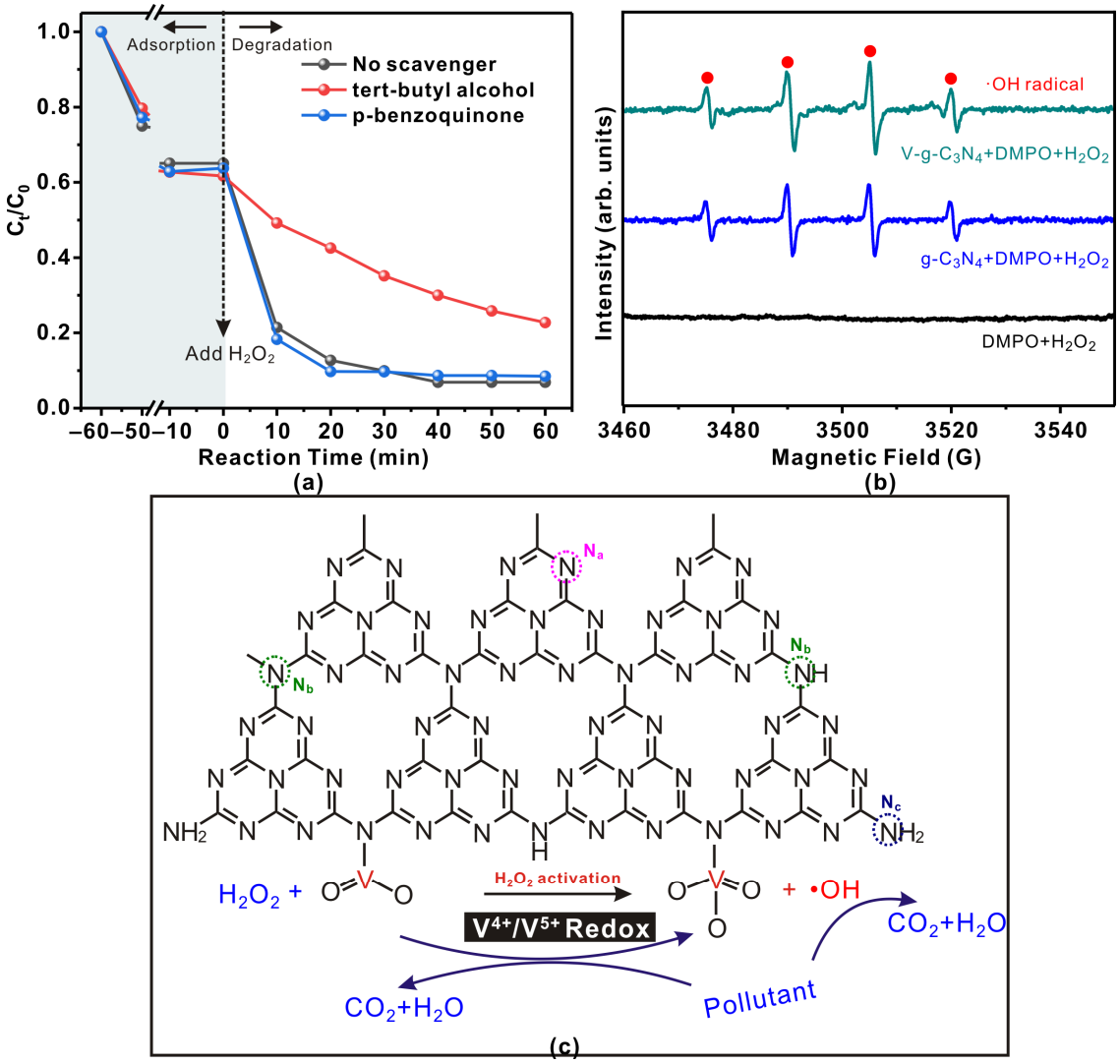

Figure 5. (**a**) Scavenger trapping experiments over V-g-C_3N_4. (**b**) EPR spectra using DMPO as the trapping reagent over V-g-C_3N_4. (**c**) A possible reaction mechanism for V-g-C_3N_4 catalyzed MB removal.

Taking all the above results together, we propose the following mechanism for V-g-C_3N_4-catalyzed MB removal (Figure 5c). The one-pot synthesized V-g-C_3N_4 consists of highly dispersed VO_2 species supported on g-C_3N_4 nanomeshes. When V-g-C_3N_4 is added into the solution, MB will rapidly adsorb onto the g-C_3N_4 nanomeshes due to its high surface area and three-dimensional interconnected structure. Once H_2O_2 is added, the Fenton-like reaction between H_2O_2 and VO_2 will produce ·OH and V^{5+}, both of which can oxidize the adsorbed MB (Figure 5c). The rapid adsorption and fast diffusion of MB over g-C_3N_4 nanomeshes, together with the efficient H_2O_2 activation involved in the V^{4+}/V^{5+} redox cycle, synergistically contribute to the superior MB removal efficiency of V-g-C_3N_4.

3. Materials and Methods

Chemicals and reagents. VCl_3 (≥99.0%) was purchased from Aladdin, Inc. (Shanghai, China). Melamine, hydrogen peroxide (H_2O_2, 30%), nitric acid (HNO_3, ~68%), and anhydrous ethanol were obtained from Sinopharm Chemical Reagents Co., Ltd. (Shanghai, China). Methylene blue (MB) was purchased from Yuanye Bio., Inc. (Shanghai, China).

Synthesis of V-g-C_3N_4. The one-pot synthesis of V-g-C_3N_4 is schematically illustrated in Scheme 1. A mixture was prepared by dispersing 3.0 g of melamine into 40 mL of ethanol, followed by the addition of 1.11 g of HNO_3 to achieve a concentration of 0.3 M in the entire reaction system. Subsequently, 355.5 mg of VCl_3 was added into the mixture. After vigorous stirring at room temperature for 60 min to ensure thorough mixing, the mixture was heated to 80 °C to fully evaporate the solvent. The solid was calcined in a covered crucible at 550 °C for 2 h under a nitrogen atmosphere. The final product was labeled as V-g-C_3N_4. Inductively coupled plasma-atomic emission spectroscopy (ICP-AES) analysis verified that the vanadium mass loading was approximately 5.0 wt%.

For comparison, g-C_3N_4 was fabricated following similar steps to V-g-C_3N_4, but without the introduction of VCl_3.

Synthesis of V-g-C_3N_4-im. Typically, 0.3 g of g-C_3N_4 was added into 40 mL of ethanol containing 48.69 mg of VCl_3. After vigorous stirring for 60 min, the mixture was heated at ~80 °C to evaporate the solvent completely. The resulting product was calcined at 550 °C for 2 h under N_2 atmosphere. ICP-AES analysis confirmed that the mass loading of vanadium was ~5.0 wt%.

Characterizations. A transmission electron microscope (TEM, JEOL JEM-1230, Tokyo, Japan) with an energy dispersive X-ray (EDX) spectroscope was used to examine the microstructure and chemical composition distribution. Morphological analysis was conducted using a Hitachi S4800 (Hitachi, Ltd. Tokyo, Japan) scanning electron microscope (SEM). The crystalline phase was analyzed using a Rigaku Ultimate IV (Rigaku Corporation, Tokyo, Japan) X-ray diffractometer (XRD) with Cu Kα radiation. A VG Scientific ESCALAB Mark II X-ray photoelectron spectrometer (XPS) was used to determine the chemical states and environment of the catalysts. Nitrogen sorption isotherms were obtained using a Micromeritics ASAP 2020 adsorption analyzer (Micromeritics Corporation, Norcross, GA, USA). The V species content was accurately verified using ICP-AES with a Profile Spec instrument. Electron paramagnetic resonance (EPR) experiments were conducted using a Bruker model A300 spectrometer (Bruker Corporation, Billerica, MA, USA) operating at 100 kHz modulation frequency at room temperature.

Catalytic activity test. Catalyst activity was assessed through a model reaction involving pollutant removal. Briefly, 10 mg of the synthesized catalyst was added to 30 mL of a methylene blue (MB) solution (15 ppm) in a 50 mL glass tube. The mixture was stirred at 25 °C for 60 min to reach the adsorption/desorption equilibrium. Afterwards, 2 mL of hydrogen peroxide (H_2O_2, 30 wt%) was rapidly added to the mixture. At predetermined time intervals, 1 mL of the suspension was extracted and centrifuged. The Shimadzu UV-3600 spectrometer was used to measure the residual MB concentration in the supernatant.

4. Conclusions

We report a one-pot synthesis of V-g-C_3N_4 nanostructures for the advanced oxidation of MB. The incorporation of vanadia species during g-C_3N_4 synthesis modifies the microstructure and surface structure of g-C_3N_4, creating a nanomesh structure with abundant amino groups (NH/NH_2). These amino groups act as anchoring sites for vanadia species, promoting high VO_2 dispersion in V-g-C_3N_4. The rapid adsorption and fast diffusion of MB over g-C_3N_4 nanomeshes, together with the efficient H_2O_2 activation into ·OH radicals via the V^{4+}/V^{5+} redox cycle, synergistically contribute to the superior MB removal efficiency of V-g-C_3N_4. Under the optimal experimental conditions, ~91% of MB was degraded by V-g-C_3N_4 within 30 min. The catalytic rate constant of V-g-C_3N_4 is 2.3-fold higher than that of V-g-C_3N_4-im. Moreover, V-g-C_3N_4 demonstrates no significant decrease in activity even after the fourth cycle, indicating its excellent stability during the pollutant removal process. Given the efficiency, cost-effectiveness, and environmentally friendly nature of the proposed one-pot synthesis, future research will investigate the scalability of this method and its applications to other dyes and pollutants.

Author Contributions: Conceptualization, J.L. and S.Z.; methodology, J.L. and K.W.; validation, Y.D. and Y.Z.; investigation, Y.D., Y.Z., K.W. and Y.W.; writing—original draft preparation, J.L.; writing—review and editing, S.Z.; visualization, J.L.; supervision, J.L. and S.Z.; project administration, J.L. and S.Z.; funding acquisition, J.L. and S.Z. All authors have read and agreed to the published version of the manuscript.

Funding: This research received financial support from the National Natural Science Foundation of China (Grant No. 22372051) and the Zhejiang Province Natural Science Foundation (Grant No. LY22B030010).

Data Availability Statement: The data presented in this study are available on request from the corresponding author.

Conflicts of Interest: The authors declare no conflicts of interest.

References

1. Ismail, G.A.; Sakai, H. Review on effect of different type of dyes on advanced oxidation processes (AOPs) for textile color removal. *Chemosphere* **2022**, *291*, 132906. [CrossRef] [PubMed]
2. Madi, K.; Chebli, D.; Ait Youcef, H.; Tahraoui, H.; Bouguettoucha, A.; Kebir, M.; Zhang, J.; Amrane, A. Green Fabrication of ZnO Nanoparticles and ZnO/rGO Nanocomposites from Algerian Date Syrup Extract: Synthesis, Characterization, and Augmented Photocatalytic Efficiency in Methylene Blue Degradation. *Catalysts* **2024**, *14*, 62. [CrossRef]
3. Li, N.; He, X.; Ye, J.; Dai, H.; Peng, W.; Cheng, Z.; Yan, B.; Chen, G.; Wang, S. H_2O_2 activation and contaminants removal in heterogeneous Fenton-like systems. *J. Hazard. Mater.* **2023**, *458*, 131926. [CrossRef] [PubMed]
4. Moreira, F.C.; Boaventura, R.A.R.; Brillas, E.; Vilar, V.J.P. Electrochemical advanced oxidation processes: A review on their application to synthetic and real wastewaters. *Appl. Catal. B* **2017**, *202*, 217–261. [CrossRef]
5. Liu, T.; Xiao, S.; Li, N.; Chen, J.; Zhou, X.; Qian, Y.; Huang, C.-H.; Zhang, Y. Water decontamination via nonradical process by nanoconfined Fenton-like catalysts. *Nat. Commun.* **2023**, *14*, 2881. [CrossRef]
6. Saravanan, A.; Deivayanai, V.C.; Kumar, P.S.; Rangasamy, G.; Hemavathy, R.V.; Harshana, T.; Gayathri, N.; Alagumalai, K. A detailed review on advanced oxidation process in treatment of wastewater: Mechanism, challenges and future outlook. *Chemosphere* **2022**, *308*, 136524. [CrossRef]
7. Wang, J.; Wang, S. Reactive species in advanced oxidation processes: Formation, identification and reaction mechanism. *Chem. Eng. J.* **2020**, *401*, 126158. [CrossRef]
8. Chen, W.; Zeng, M.; Yang, J. Preparation of Fenton Catalysts for Water Treatment. *Catalysts* **2023**, *13*, 1407. [CrossRef]
9. Rana, A.G.; Tasbihi, M.; Schwarze, M.; Minceva, M. Efficient Advanced Oxidation Process (AOP) for Photocatalytic Contaminant Degradation Using Exfoliated Metal-Free Graphitic Carbon Nitride and Visible Light-Emitting Diodes. *Catalysts* **2021**, *11*, 662. [CrossRef]
10. Yamaguchi, R.; Kurosu, S.; Suzuki, M.; Kawase, Y. Hydroxyl radical generation by zero-valent iron/Cu (ZVI/Cu) bimetallic catalyst in wastewater treatment: Heterogeneous Fenton/Fenton-like reactions by Fenton reagents formed in-situ under oxic conditions. *Chem. Eng. J.* **2018**, *334*, 1537–1549. [CrossRef]
11. Hussain, S.; Aneggi, E.; Goi, D. Catalytic activity of metals in heterogeneous Fenton-like oxidation of wastewater contaminants: A review. *Environ. Chem. Lett.* **2021**, *19*, 2405–2424. [CrossRef]
12. Ricardo, I.A.; Alberto, E.A.; Silva Júnior, A.H.; Macuvele, D.L.P.; Padoin, N.; Soares, C.; Gracher Riella, H.; Starling, M.C.V.M.; Trovó, A.G. A critical review on microplastics, interaction with organic and inorganic pollutants, impacts and effectiveness of advanced oxidation processes applied for their removal from aqueous matrices. *Chem. Eng. J.* **2021**, *424*, 130282. [CrossRef]

13. Liu, Y.; Wang, J. Multivalent metal catalysts in Fenton/Fenton-like oxidation system: A critical review. *Chem. Eng. J.* **2023**, *466*, 143147. [CrossRef]
14. Cheng, C.; Ren, W.; Miao, F.; Chen, X.; Chen, X.; Zhang, H. Generation of Fe^{IV}=O and its Contribution to Fenton-Like Reactions on a Single-Atom Iron−N−C Catalyst. *Angew. Chem. Int. Ed.* **2023**, *62*, e202218510. [CrossRef] [PubMed]
15. Gu, C.-H.; Pan, Y.; Wei, T.-T.; Zhang, A.-Y.; Si, Y.; Liu, C.; Sun, Z.-H.; Chen, J.-J.; Yu, H.-Q. Upcycling waste sewage sludge into superior single-atom Fenton-like catalyst for sustainable water purification. *Nat. Water* **2024**, *2*, 649–662. [CrossRef]
16. Sauer, T.P.; Casaril, L.; Oberziner, A.L.B.; José, H.J.; Moreira, R.d.F.P.M. Advanced oxidation processes applied to tannery wastewater containing Direct Black 38—Elimination and degradation kinetics. *J. Hazard. Mater.* **2006**, *135*, 274–279. [CrossRef]
17. Zubir, N.A.; Yacou, C.; Zhang, X.; Diniz da Costa, J.C. Optimisation of graphene oxide–iron oxide nanocomposite in heterogeneous Fenton-like oxidation of Acid Orange 7. *J. Environ. Chem. Eng.* **2014**, *2*, 1881–1888. [CrossRef]
18. Ling, L.; Liu, Y.; Pan, D.; Lyu, W.; Xu, X.; Xiang, X.; Lyu, M.; Zhu, L. Catalytic detoxification of pharmaceutical wastewater by Fenton-like reaction with activated alumina supported CoMnAl composite metal oxides catalyst. *Chem. Eng. J.* **2020**, *381*, 122607. [CrossRef]
19. Bouzayani, B.; Sanromán, M.Á. Polymer-Supported Heterogeneous Fenton Catalysts for the Environmental Remediation of Wastewater. *Molecules* **2024**, *29*, 2188. [CrossRef] [PubMed]
20. Lee, D.W.; Yoo, B.R. Advanced metal oxide (supported) catalysts: Synthesis and applications. *J. Ind. Eng. Chem.* **2014**, *20*, 3947–3959. [CrossRef]
21. Munnik, P.; de Jongh, P.E.; de Jong, K.P. Recent Developments in the Synthesis of Supported Catalysts. *Chem. Rev.* **2015**, *115*, 6687–6718. [CrossRef] [PubMed]
22. Flytzani-Stephanopoulos, M.; Gates, B.C. Atomically Dispersed Supported Metal Catalysts. *Ann. Rev. Chem. Biomol. Eng.* **2012**, *3*, 545–574. [CrossRef]
23. Wei, Q.-X.; Zhang, A.-Y.; Yang, Z.; Hu, S.; Wang, D.-J.; Zhang, C.; Liu, C.; Liu, R. Oxygen-exfoliated cobalt-doped C_3N_4 for superior Fenton-like catalysis: The accessible metal exposure and synergistic pollutant adsorption from three-dimensional layered configuration. *J. Environ. Chem. Eng.* **2023**, *11*, 111067. [CrossRef]
24. Védrine, J.C. Recent developments and prospectives of acid-base and redox catalytic processes by metal oxides. *Appl. Catal. A* **2019**, *575*, 170–179. [CrossRef]
25. Li, J.; Zahid, M.; Sun, W.; Tian, X.; Zhu, Y. Synthesis of Pt supported on mesoporous g-C_3N_4 modified by ammonium chloride and its efficiently selective hydrogenation of furfural to furfuryl alcohol. *Appl. Surf. Sci.* **2020**, *528*, 146983. [CrossRef]
26. Zhang, Y.-x.; Guo, X.-y.; Liu, B.; Zhang, J.-l.; Gao, X.-h.; Ma, Q.-x.; Fan, S.-b.; Zhao, T.-s. Surface modification of g-C_3N_4-supported iron catalysts for CO hydrogenation: Strategy for product distribution. *Fuel* **2021**, *305*, 121473. [CrossRef]
27. Inagaki, M.; Tsumura, T.; Kinumoto, T.; Toyoda, M. Graphitic carbon nitrides (g-C_3N_4) with comparative discussion to carbon materials. *Carbon* **2019**, *141*, 580–607. [CrossRef]
28. Yuan, M.; Yuan, H.; Xun, S.; Le, R.; Huang, Y.; He, M.; Zhu, L.; Zhu, W.; Li, H. VO_2 uniformly supported by 3D g-C_3N_4: A highly effective catalyst for deep oxidative desulfurization. *Fuel* **2022**, *319*, 123792. [CrossRef]
29. Tian, N.; Zhang, Y.; Li, X.; Xiao, K.; Du, X.; Dong, F.; Waterhouse, G.I.N.; Zhang, T.; Huang, H. Precursor-reforming protocol to 3D mesoporous g-C_3N_4 established by ultrathin self-doped nanosheets for superior hydrogen evolution. *Nano Energy* **2017**, *38*, 72–81. [CrossRef]
30. Reddy, I.N.; Reddy, L.V.; Jayashree, N.; Reddy, C.V.; Cho, M.; Kim, D.; Shim, J. Vanadium-doped graphitic carbon nitride for multifunctional applications: Photoelectrochemical water splitting and antibacterial activities. *Chemosphere* **2021**, *264*, 128593. [CrossRef]
31. Cheng, W.; Zeng, G.; Niederberger, M. Design of vanadium oxide core–shell nanoplatelets for lithium ion storage. *J. Mater. Chem. A* **2015**, *3*, 2861–2868. [CrossRef]
32. Huang, B.L.; Zhang, H.; Qiu, Z.; Liu, P.; Cao, F.; He, X.; Xia, Y.; Liang, X.; Wang, C.; Wan, W.; et al. Hyphae Carbon Coupled with Gel Composite Assembly for Construction of Advanced Carbon/Sulfur Cathodes for Lithium–Sulfur Batteries. *Small* **2024**, *20*, 2307579. [CrossRef] [PubMed]
33. Liu, J.; Yin, H.; Nie, Q.; Zou, S. Highly Dispersed Vanadia Anchored on Protonated g-C_3N_4 as an Efficient and Selective Catalyst for the Hydroxylation of Benzene into Phenol. *Molecules* **2022**, *27*, 6965. [CrossRef] [PubMed]
34. Alcudia-Ramos, M.A.; Fuentez-Torres, M.O.; Ortiz-Chi, F.; Espinosa-González, C.G.; Hernández-Como, N.; García-Zaleta, D.S.; Kesarla, M.K.; Torres-Torres, J.G.; Collins-Martínez, V.; Godavarthi, S. Fabrication of g-C_3N_4/TiO_2 heterojunction composite for enhanced photocatalytic hydrogen production. *Ceram. Int.* **2020**, *46*, 38–45. [CrossRef]
35. Balakhonov, S.V.; Efremova, M.V.; Ivanov, V.K.; Churagulov, B.R. Facile synthesis of vanadia aerogels with controlled V^{3+}/V^{4+} ratio. *Mater. Lett.* **2015**, *156*, 109–112. [CrossRef]
36. Liu, J.; Zou, S.; Lou, B.; Chen, C.; Xiao, L.; Fan, J. Interfacial Electronic Interaction Induced Engineering of ZnO-BiOI Heterostructures for Efficient Visible-Light Photocatalysis. *Inorg. Chem.* **2019**, *58*, 8525–8532. [CrossRef]
37. Shoran, S.; Dahiya, S.; Rani, M.; Nehra, S.P.; Sharma, A.; Chaudhary, S. Synergistic photocatalysis of VO_2-A/g-C_3N_4 composites for efficient degradation of anionic and cationic dyes: Towards a sustainable environmental solution. *Appl. Surf. Sci.* **2025**, *684*, 161852. [CrossRef]
38. Adeleke, J.T.; Theivasanthi, T.; Thiruppathi, M.; Swaminathan, M.; Akomolafe, T.; Alabi, A.B. Photocatalytic degradation of methylene blue by ZnO/$NiFe_2O_4$ nanoparticles. *Appl. Surf. Sci.* **2018**, *455*, 195–200. [CrossRef]

39. Oladoye, P.O.; Ajiboye, T.O.; Omotola, E.O.; Oyewola, O.J. Methylene blue dye: Toxicity and potential elimination technology from wastewater. *Results Eng.* **2022**, *16*, 100678. [CrossRef]
40. Liu, J.; Yin, H.; Nie, Q.; Wang, H.; Zhou, J.; Zou, S. Encapsulating Mn_3O_4 Nanorods in a Shell of SiO_2 Nanobubbles for Confined Fenton-Type Catalysis. *Inorg. Chem.* **2021**, *60*, 16658–16665. [CrossRef]
41. Jia, H.; Liu, Q.; Si, J.; Chen, Y.; Zhou, G.; Lan, H.; He, W. Oxidation engineering triggered peroxidase-like activity of VO_xC for detection of dopamine and glutathione. *Nanoscale Adv.* **2023**, *5*, 5799–5809. [CrossRef] [PubMed]
42. Jin, L.; Liu, H.; Ye, L.; Huang, Y.; Liu, X.; Huang, D. Revealing the primary role of the V^{4+}/V^{5+} cycle in $InVO_4$ catalysts for promoting the photo-Fenton reaction. *Environm. Sci. Nano* **2024**, *11*, 942–950. [CrossRef]
43. Du, G.; Espenson, J.H. Oxidation of Vanadium(III) by Hydrogen Peroxide and the Oxomonoperoxo Vanadium(V) Ion in Acidic Aqueous Solutions: A Kinetics and Simulation Study. *Inorg. Chem.* **2005**, *44*, 5514–5522. [CrossRef] [PubMed]